

# Complex fault system revealed from 3-D seismic reflection data with deep learning and fault network analysis

Thilo Wrona<sup>1,2\*</sup>, Indranil Pan<sup>3,4,5</sup>, Rebecca E. Bell<sup>6</sup>, Christopher A-L. Jackson<sup>7</sup>, Robert L. Gawthorpe<sup>1</sup>, Haakon Fossen<sup>8</sup>, Edoseghe E. Osagiede<sup>1</sup>, and Sascha Brune<sup>2,9</sup>

<sup>1</sup>Department of Earth Science, University of Bergen, Allégaten 41, N-5007 Bergen, Norway.

<sup>2</sup>GFZ German Research Centre for Geosciences, Telegrafenberg, 14473 Potsdam, Germany.

<sup>3</sup>Centre for Process Systems Engineering & Centre for Environmental Policy, Imperial College London, UK.

<sup>4</sup>The Alan Turing Institute, British Library, London, UK.

<sup>5</sup>School of Mathematics, Statistics & Physics, Newcastle University, UK.

<sup>6</sup>Basins Research Group (BRG), Department of Earth Science and Engineering, Imperial College, Prince Consort Road, London, SW7 2BP, UK.

<sup>7</sup>Department of Earth and Environmental Sciences, University of Manchester, Manchester, UK

<sup>8</sup>Museum of Natural History, University of Bergen, Allégaten 41, N-5007 Bergen, Norway.

<sup>9</sup>Institute of Geosciences, University of Potsdam, Potsdam-Golm, Germany.

\*[wrona@gfz-potsdam.de](mailto:wrona@gfz-potsdam.de)

## ABSTRACT

Understanding where normal faults are is critical to an accurate assessment of seismic hazard, the successful exploration for and production of natural (including low-carbon) resources, and for the safe subsurface storage of CO<sub>2</sub>. Our current knowledge of normal fault systems is largely derived from seismic reflection data imaging intra-continental rifts and continental margins. However, exploitation of these data is limited by interpretation biases, data coverage and resolution, restricting our understanding of fault systems. Applying supervised deep learning to one of the largest offshore 3-D seismic reflection data sets from the northern North Sea allows us to image the complexity of the rift-related fault system. The derived fault score volume allows us to extract almost 8000 individual normal faults of different geometries, which together form an intricate network characterised by a multitude of splays, junctions and intersections. Combining tools from deep learning, computer vision and network analysis allows us to map and analyse the fault system in great detail and a fraction of the time required by conventional interpretation methods. As such, this study shows how we can efficiently identify and analyse fault systems in increasingly large 3-D seismic data sets.

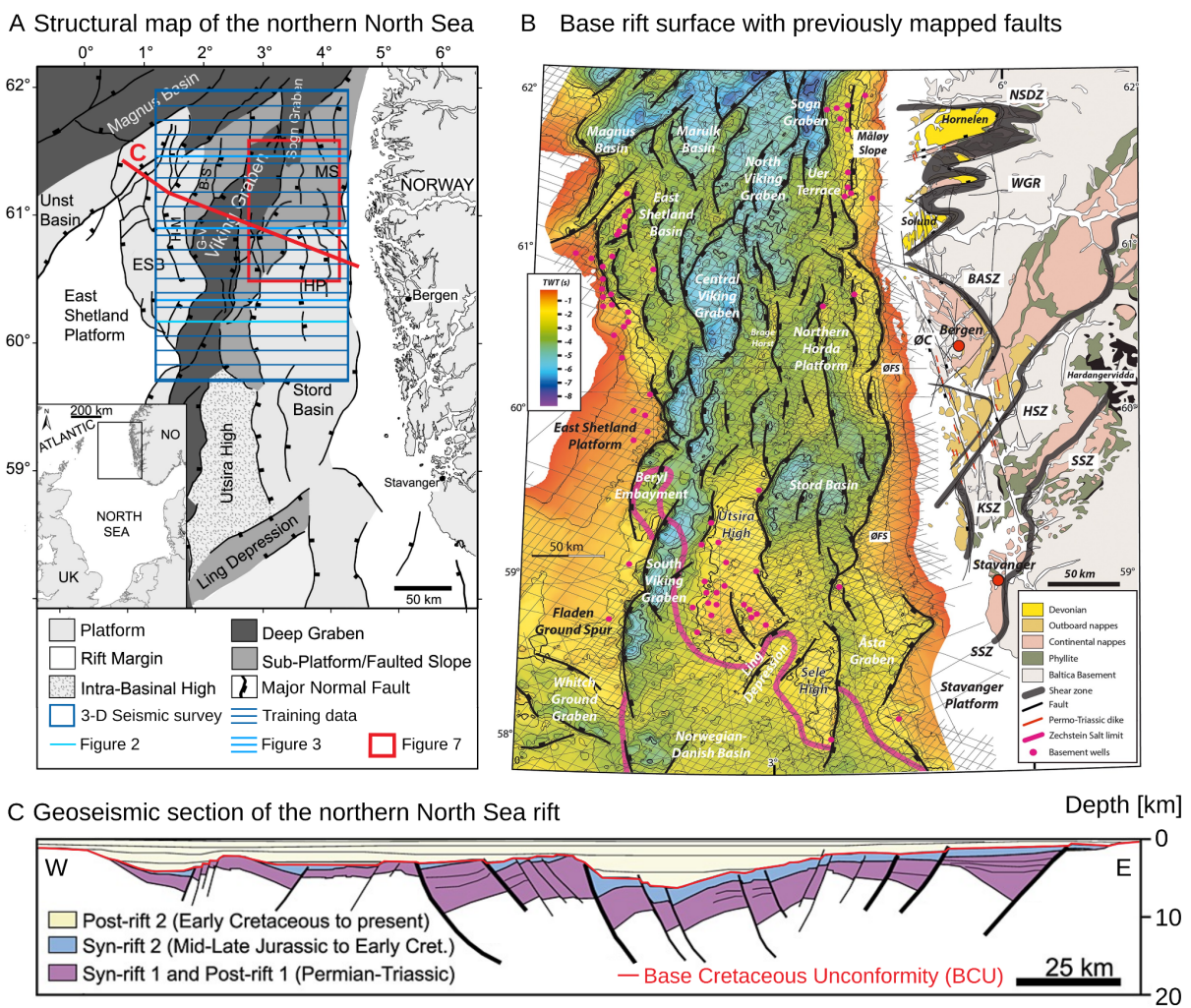
## 37 1. INTRODUCTION

38         Understanding the geometry and growth of normal fault systems is critical when assessing  
39 seismic hazard, when identifying suitable sites for subsurface CO<sub>2</sub> storage and when exploring for  
40 natural resources (traditional and low-carbon). For example, whereas probabilistic seismic hazard  
41 analyses based on seismic event catalogues are extremely useful when trying to forecast earthquake  
42 likelihood and location, high-resolution fault mapping, preferably in 3-D, can help us constrain the  
43 slip tendency of faults, where seismic catalogues are discontinuous and/or incomplete (e.g. Morris et  
44 al., 1996; Moeck et al., 2009; Yukutake et al., 2015). Moreover, faults can facilitate (or impede) fluid  
45 and gas migration to the Earth's surface, thus determining their geometry and connectivity, as well as  
46 their hydraulic properties is key for assessing their role in the long-term subsurface storage of CO<sub>2</sub>  
47 (Bissell et al., 2011; Kampman et al., 2014). In both of these examples, we need robust predictions of  
48 3-D fault geometry over large areas and across a wide range of scales (100s m to 100 km).

49         Accurately mapping fault systems in 2-D and 3-D seismic reflection data typically requires  
50 expertise and time (e.g. Bond, 2015). While we can map fault systems in great detail over small areas  
51 using 3-D seismic reflection data (e.g. Lohr et al., 2008; Wrona et al., 2017; Claringbould et al.,  
52 2020), we lack an understanding of the character of 3-D fault populations at the scale of entire rift  
53 systems, as regional studies are often limited to only sparse, 2-D seismic sections (e.g. Clerc et al.,  
54 2015; Fazlikhani et al., 2017; Phillips et al., 2019). 3-D numerical models are now capable of  
55 simulating fault networks at the rift scale; however, there are few observational data sets of the same  
56 scale to test the predictions of these models and, therefore, help refine them (e.g. Naliboff et al., 2020;  
57 Pan et al., 2021).

58         Supervised deep learning allows us to map faults in seismic reflection data (e.g. Wu et al.,  
59 2019; Mosser et al., 2020; Wrona et al., 2021a), but up until now many of these studies have laid the  
60 foundation by focusing on detecting faults rather than studying the geometry of these faults. In this  
61 study, by applying supervised deep learning to newly-acquired broadband 3-D seismic reflection data

65 imaging much of the northern North Sea rift (161 km wide in E-W, 266 km long area in N-S, 0-20 km  
 66 deep), we map the fault network associated with a continental rift basin at an unprecedented level of  
 67 detail. Using manually labelled data (<0.1% of data volume), we train a deep convolutional neural  
 68 network (U-Net) to predict faults in our data set. The predicted score ranges from 0 (no fault) to 1  
 69 (fault). Based on this score across the entire 3-D seismic volume we employ a second workflow to  
 70 extract the normal fault system as a network (a set of nodes and edges) allowing us to investigate the  
 71 architecture and growth of this extremely complex system consisting of thousands of intersecting  
 72 faults.



73  
 74 **Figure 1:** A Structural overview map of the northern North Sea basin system (from Tillmans et al.,  
 75 2021 after Færseth, 1996). Blue rectangle marks the outline of the seismic survey in this study. ESB =  
 76 East Shetland Basin, B-S = Brent-Statfjord Fault, G-V = Gullfaks-Visund Fault, MS = Måløy Slope,  
 77 HP = Horda Platform. **B** The base rift surface (base Permo-Triassic rifting) time-structure map in the  
 78 northern North Sea rift (from Fazlikhani et al., 2017) and the geology of southwestern Norway,  
 79 showing the general onshore and offshore structural configuration in the study area. Bold black lines

80 highlight major rift-related normal faults displacing the base rift surface where all units older than  
81 Upper Permian are considered basement. Black lines in the background show some of the 2-D seismic  
82 reflection surveys used by Fazlikhani et al. (2017). NSDZ, Nordfjord-Sogn Detachment Zone; BASZ,  
83 Bergen Arc Shear Zone; WGR, Western Gneiss Region; ØC, Øygarden Complex (gneiss); ØFS,  
84 Øygarden Fault System; HSZ, KSZ, and; SSZ: Hardangerfjord, Karmøy, and Stavanger shear zones,  
85 respectively. C Regional interpretation of the structure of the northern North Sea after Færseth (1996).

## 86 2. GEOLOGICAL SETTING

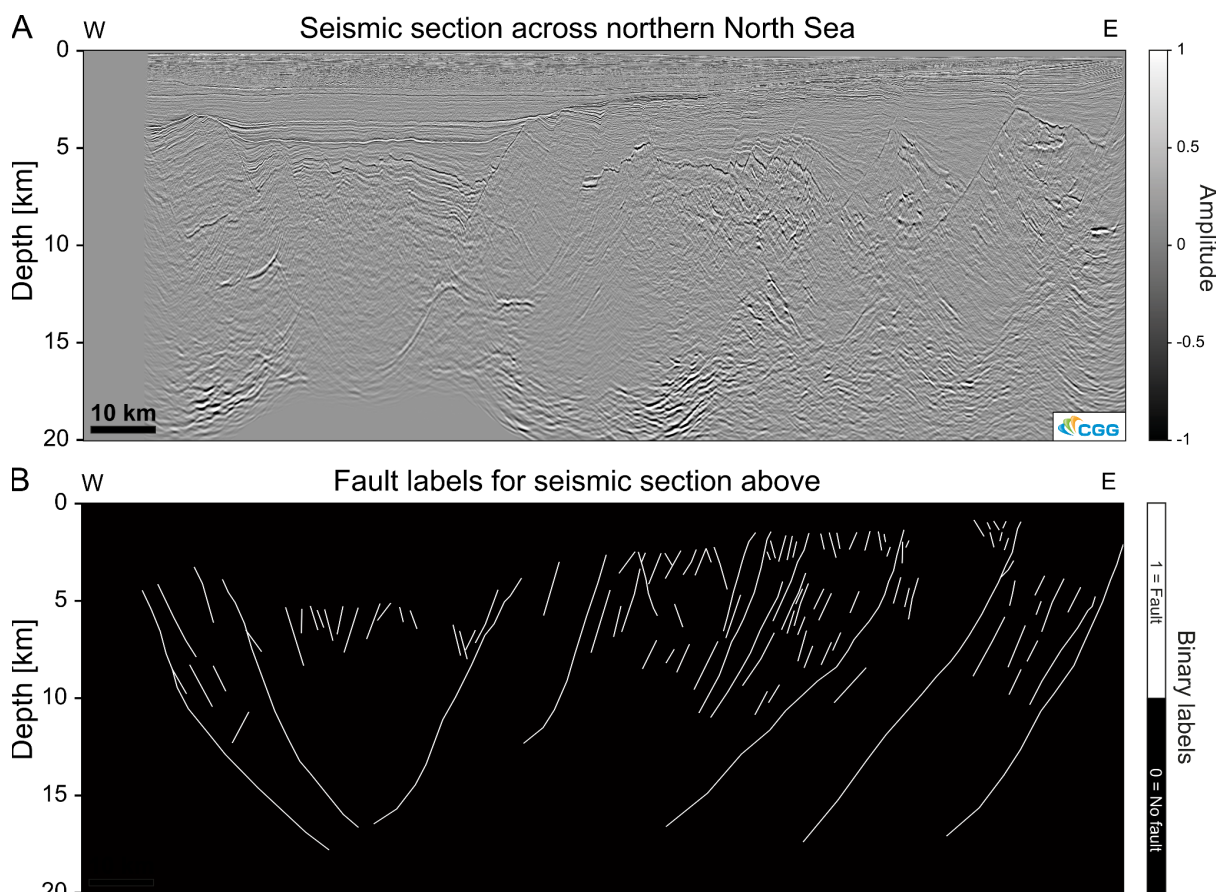
87 The study area is located in the northern North Sea (Fig. 1), where continental crust consists of  
88 10–30-km-thick crystalline basement overlain by as much as 12 km of sedimentary strata deposited  
89 during, after, and possibly even before periods of rifting in the late Permian–Early Triassic (rift phase  
90 1) and Middle Jurassic–Early Cretaceous (rift phase 2) (e.g. Whipp et al., 2014; Bell et al., 2014;  
91 Maystrenko et al., 2017). The extension direction of these two phases has long been debated. Whereas  
92 most studies agree that the late Permian–Early Triassic rifting was driven by E-W extension (e.g.  
93 Færseth et al., 1997; Torsvik et al., 1997), Middle Jurassic–Early Cretaceous rifting has been  
94 associated with both E-W (e.g. Bartholomew et al., 1993; Brun and Tron, 1993) and NW-SE  
95 extension (e.g. Færseth, 1996; Doré et al., 1997; Færseth et al., 1997) (Fig. 1B). This debate is further  
96 complicated by the fact that some of the largest normal faults on the Horda Platform developed during  
97 rift phase 1, but were subsequently reactivated during rift phase 2 (e.g. Whipp et al., 2014; Bell et al.,  
98 2014). The crystalline basement underlying the sedimentary strata formed by terrane accretion during  
99 the Sveconorwegian (1140–900 Ma) and Caledonian (460–400 Ma) orogenies (Bingen et al., 2008).  
100 Several studies argue that this structural template, in particular the ductile shear zones, controlled the  
101 location, strike, and overall pattern of rift-related faulting in the overlying sedimentary successions  
102 being reactivated as normal faults, or by limiting the along-strike propagation of faults (e.g.  
103 Fazlikhani et al., 2017; Phillips et al., 2019; Osagiede et al., 2020; Wiest et al., 2020).

## 104 3. DATA & METHODS

### 105 3.1. 3-D seismic reflection data

106 In this study, we use one of the largest offshore 3-D seismic data sets ever acquired, which  
107 images a large part of the northern North Sea rift across an area of 35,410 km<sup>2</sup>, and with excellent  
108 depth-imaging down to 22 km (i.e., the middle-to-lower crust) (Figs. 1, 2A, 3). The data set was

109 acquired using eight, up to 8-km-long streamers that were towed ~40 m below the water surface. The  
 110 broadseis technology used for recording covers a wide range of frequencies (2.5-155 Hz), providing  
 111 high-resolution depth imaging. The data were binned at  $12.5 \times 18.75$  m, with a vertical sample rate of  
 112 4 ms. The data was 3-D true amplitude prestack depth-migrated. The seismic volume was zero-phase  
 113 processed with SEG normal polarity; i.e., a positive reflection (white) corresponds to an acoustic  
 114 impedance (density  $\times$  velocity) increase with depth. More details on data acquisition and pre-  
 115 processing steps are provided by Wrona et al., (2019, 2021a).

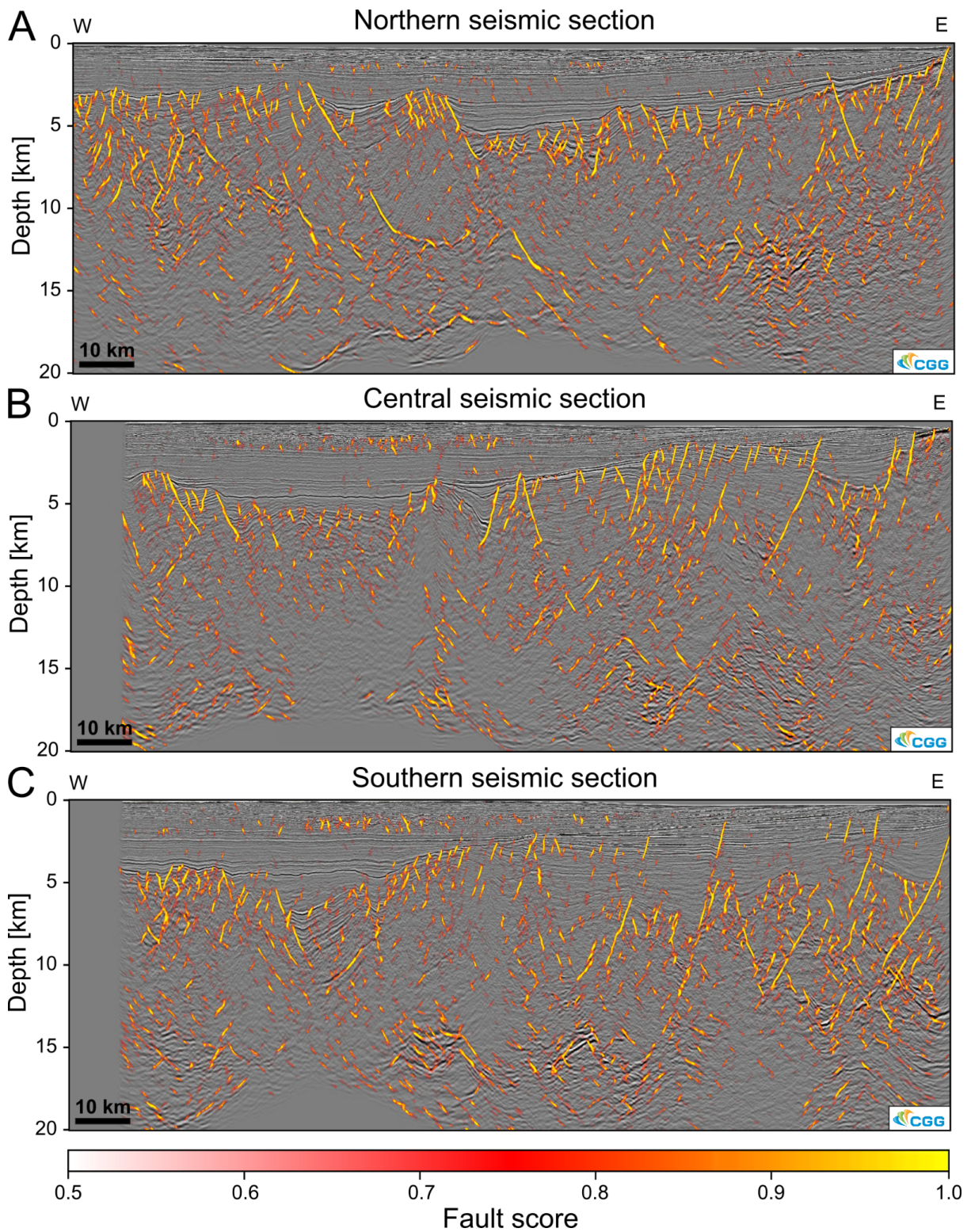


116 **Figure 2:** **A** Example seismic section across the northern North Sea. Amplitudes are scaled for  
 117 machine learning **B** Example of fault interpretation of the section used to train a deep convolutional  
 118 neural network for fault prediction.  
 119

## 120 3.2. Deep learning

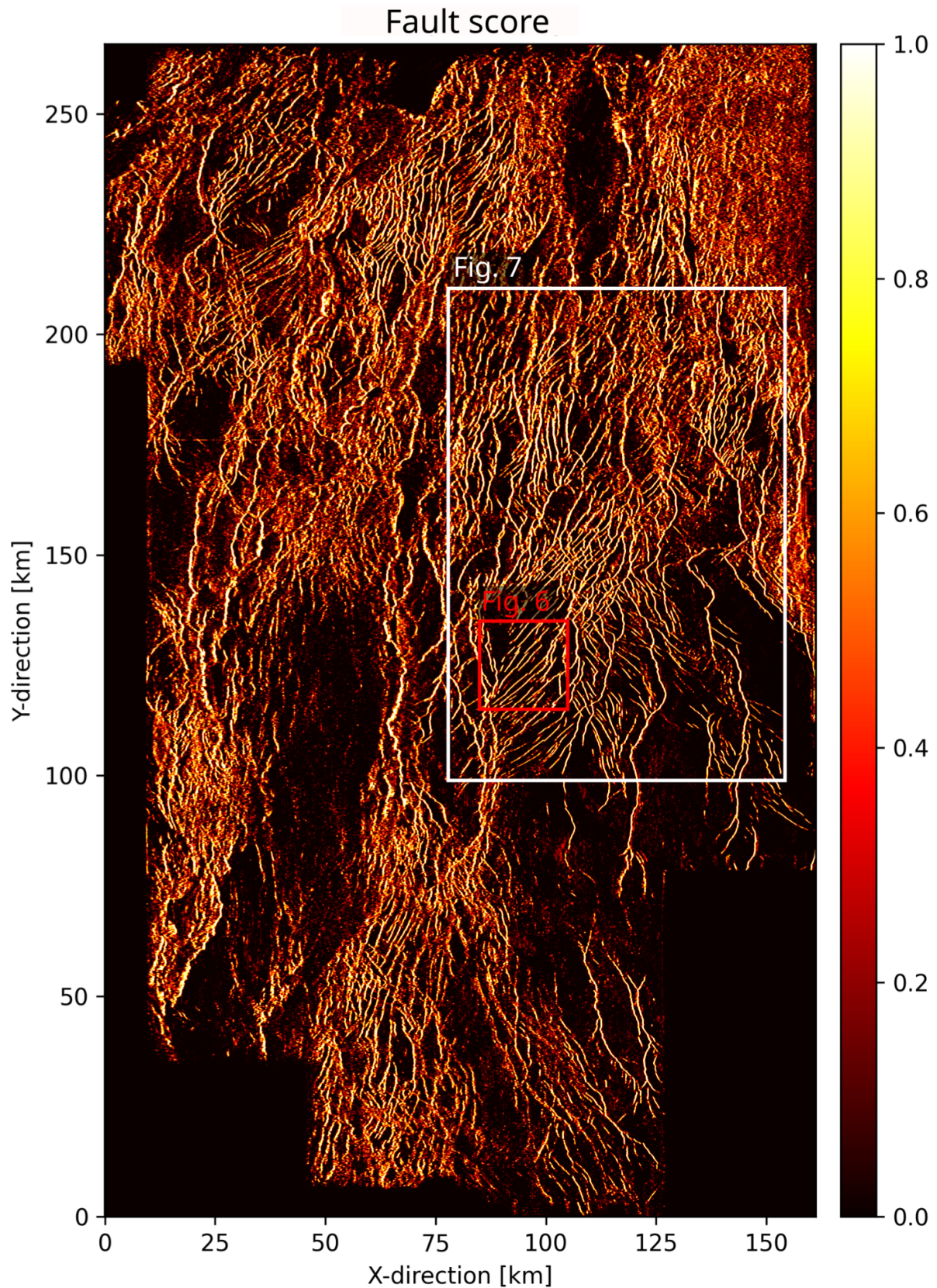
121 Deep learning describes a set of algorithms and models, which learn to perform a specific task  
 122 (e.g. fault interpretation) on a given data set without explicit feature engineering (e.g. the calculation  
 123 and calibration of seismic attributes, such as coherence or variance). Deep learning allows the

124 derivation of a fault score volume that highlights normal faults within a 3-D seismic volume. This  
125 approach requires that a large number of examples of faults and unfaulted strata are labelled in the  
126 training seismic data. We extract 80,000 such examples (2-D squares of 128×128 pixels) from 22  
127 interpreted seismic sections oriented perpendicular to the N-trending rift (Figs. 1A, 2). Note that these  
128 seismic sections only constitute <0.1% of the entire 3-D seismic volume. Next, we split these  
129 examples into three groups; one set for training (80%), one for validation (10%), and one for testing  
130 (10%). We use the first of these to train a deep convolutional neural network (U-Net) designed to  
131 perform image segmentation tasks (Ronneberger et al., 2015). Using the validation set, we track the  
132 accuracy and loss of the model during training and stop once the validation loss does not decrease  
133 further. Finally, we apply the model to the entire 3-D seismic volume to derive a fault score volume  
134 (Figs. 3, 4), an attribute, which ranges from 0 (no fault) to 1 (fault). All details of the workflow and  
135 the code are provided by Wrona et al. (2021b, 2021a).



136  
 137  
 138  
 139  
 140

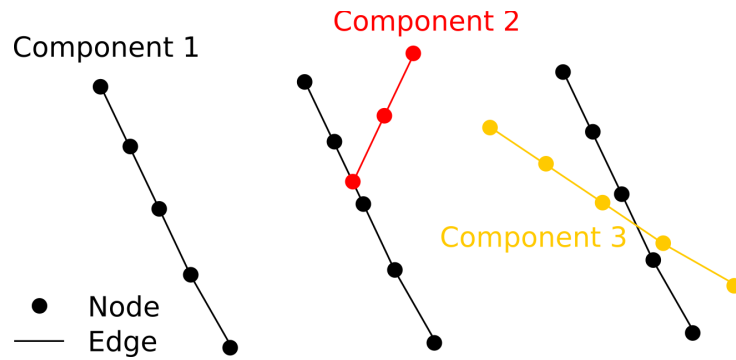
**Figure 3:** Examples of seismic sections extracted from fault score volume of the 3-D seismic data set. Note that these sections were not part of the training data, but are actually 6.25 km away from the closest interpreted seismic section (see Fig. 1A).



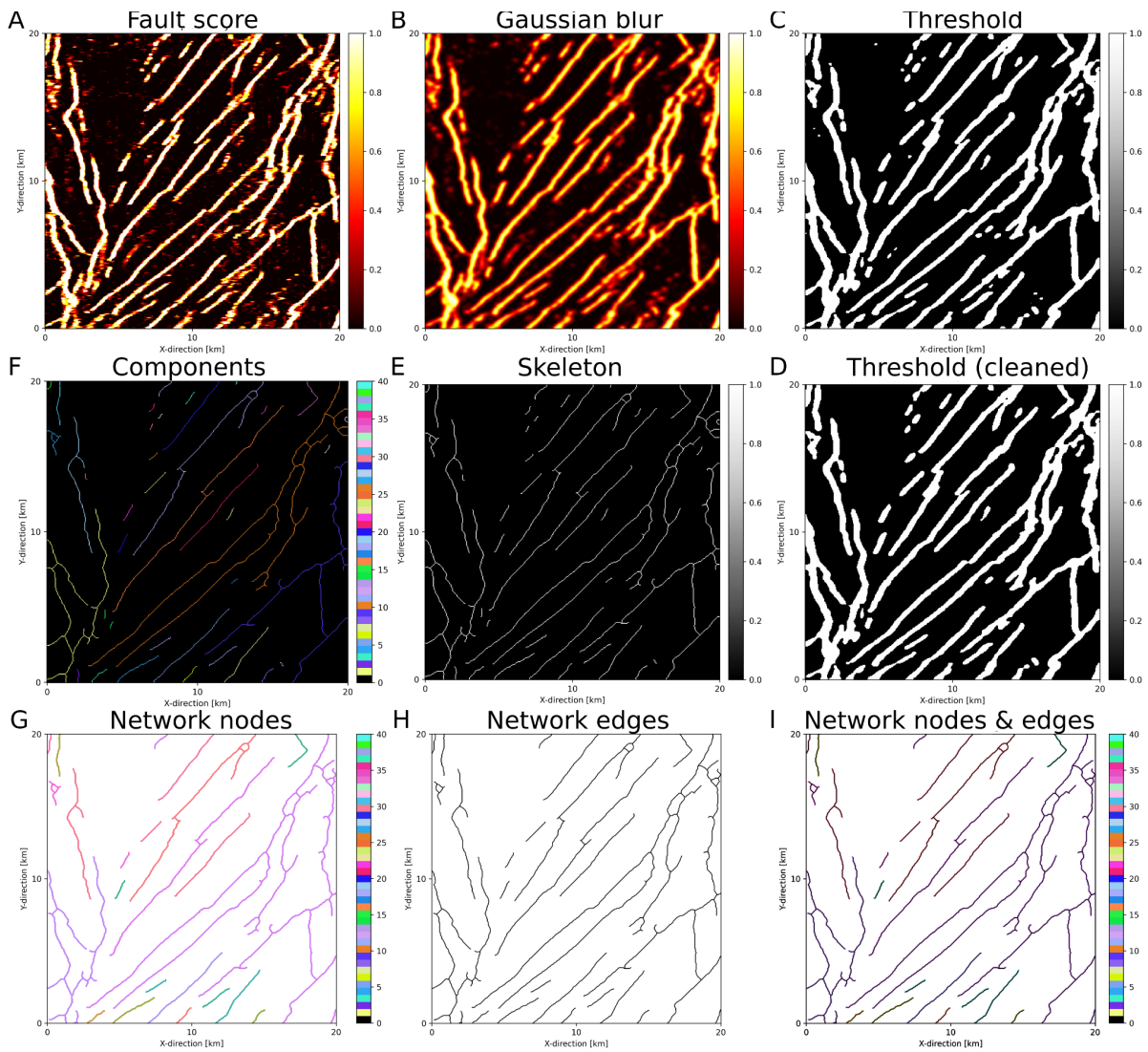
141  
 142 **Figure 4:** Surface capturing tectonic faults extracted from fault likelihood volume. The surface was  
 143 extracted 500 m below the Base Cretaceous Unconformity, where we observe a large number of  
 144 faults, which were either formed or reactivated in the second rift phase. White rectangle shows the



145 area used for validation (Fig. 8) and the red rectangle indicates the area where we demonstrate our  
 146 fault network extraction workflow (Fig. 6).



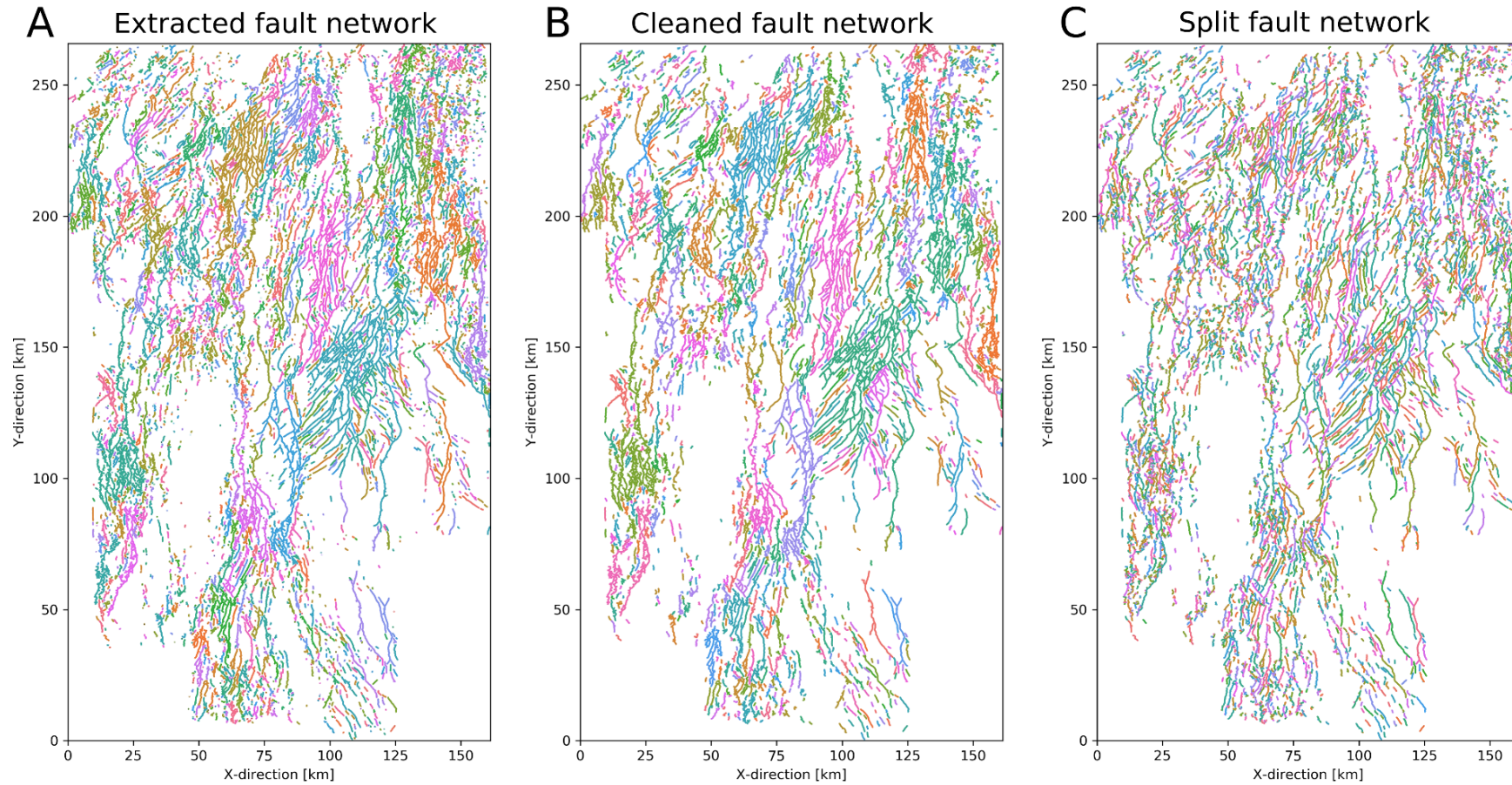
147  
 148 **Figure 5:** Schematic illustration of fault network (or graph) with nodes, edges and components. Each  
 149 node marks a location along the fault. Each edge connects two nodes and each (connected) component  
 150 indicates all nodes connected to one another by edges.  
 151



152  
 153 **Figure 6:** Fault network extraction workflow showing: **A** Fault score extracted along the surface (500  
 154 m below BCU). **B** Gaussian Blur filter ( $\sigma=2$ ) of surface. **C** Threshold (0.35) of filter. **D** Cleaned

155 threshold where small patches are removed. **E** Skeleton of cleaned threshold. **F** Connected  
156 components of skeleton. **G** Network nodes based on components. **H** Network edges based on  
157 components. **I** Network nodes and edges combined. Note that colours in F, G and I indicate connected  
158 components (i.e. individual faults), before splitting (see Fig. 6).

## Fault network editing



159

160 **Figure 7: A** Fault network extracted from BCU (Fig. 4D). Note the large areas with the same colours resulting from multiple faults being grouped into one

161 connected component **B** Fault network after removal of noise (i.e. small components). **C** Fault network after splitting junctions previously connecting

162 splaying and intersecting faults. Note that large connected components are split up and individual faults are highlighted by different colours.

### 163 3.3. Automated fault network extraction and analysis

164         Extracting a fault network from the 3-D volume allows us to perform a comprehensive  
165 geometric analysis of the fault system using our fault analysis toolbox - fatbox (Wrona et al., 2022).  
166 The basic idea is to describe a fault system in 2-D as a network (or graph), i.e. sets of nodes and edges  
167 (Fig. 5). Each node marks a location along the fault and each edge connects two nodes. All nodes  
168 connected to one another by edges are labelled as a (connected) component.

169         Our fault extraction workflow consists of these eight steps: (1) extract horizon, (2) Gaussian  
170 blur filter, (3) thresholding, (4) cleaning, (5) skeletonization, (6) connect components, (7) add nodes  
171 to graph, (8) add edges to graph and (9) split junctions. While applying it to our North Sea target  
172 region, we first attempt to capture as many faults as possible by extracting the fault score along a  
173 horizon 500 m below Base Cretaceous Unconformity (BCU) (Fig. 1C). Here we observe a large  
174 number of faults, which were either formed in the second rift phase, or formed in the first rift phase  
175 and reactivated in the second rift phase (Figs. 4, 6A). Second, we apply a Gaussian blur filter to  
176 increase lateral fault continuity (Fig. 6B). Third, we apply a threshold of 0.35 to separate the faults  
177 from the background in the fault likelihood (Fig. 6C). This threshold is a tradeoff, which balances  
178 capturing as many faults as possible (lower values) and identifying clearly resolvable faults (high  
179 values). Four, we further restrict this threshold and essentially filter these points by removing areas  
180 smaller than 25 pixels (Fig. 6D). Five, we collapse the faults to one-pixel wide lines using  
181 skeletonization (Guo and Hall, 1992) (Fig. 6E). Six, we label adjacent pixels in the image as  
182 connected components (Wu et al., 2009) (Fig. 6F). Each component consists of pixels which are  
183 connected to each other. These components represent the faults in the network. At this point, we can  
184 build our graph using these connected components of the image (Fig. 6F). Each pixel belonging to a  
185 component becomes a node whereas edges are created between neighbouring nodes (Fig 6G-I). This  
186 process results in a number of faults with splays, junctions or intersections being grouped into one  
187 connected component (Fig. 7A). To correct this, we split up junctions (nodes with three edges) based  
188 on the similarity of strike, i.e. aligned branches remain connected (Fig. 7B,C). This final network is  
189 compared to the Base Late Jurassic horizon mapped by Tillmans et al., (2021) (Fig. 8). Additionally,

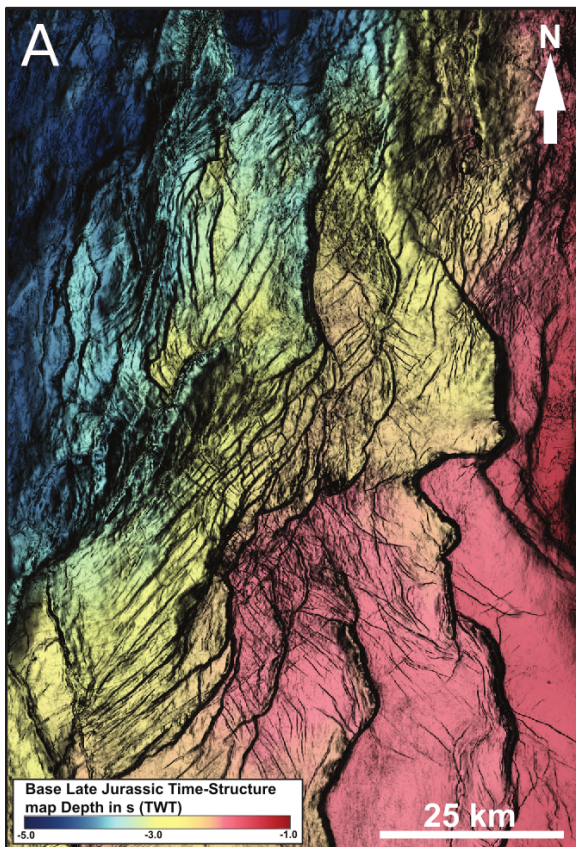
190 we perform the exact same workflow on ten slices through the fault score volume (1-10 km depth) to  
191 capture 3-D fault geometries with depth (Fig. 9).

192 After extracting the fault system, we calculate a series of typical fault properties using our fault  
193 analysis toolbox - fatbox (Wrona et al., 2022) (Fig. 10). First, we calculate the fault length as the sum  
194 of the edge lengths of each component (Fig. 10B). Second, we calculate the strike along the fault from  
195 neighbouring nodes (Fig. 10C). If we were to calculate the overall fault strike, we would overlook  
196 along-strike variations in strike. If we were to calculate the strike as the orientation of each edge, we  
197 would only obtain values of 0, 45 or 90°, because the nodes are closely spaced. Instead, we calculate  
198 the strike from the 3rd degree neighbouring nodes (i.e. neighbours of neighbours of neighbours). This  
199 assures a robust, high resolution fault strike calculation. Combining the fault length and strike, we can  
200 generate a length-weighted Rose diagram (Fig. 10C). Finally, we calculate the fault density as the  
201 fault length per area (Fig. 10D).

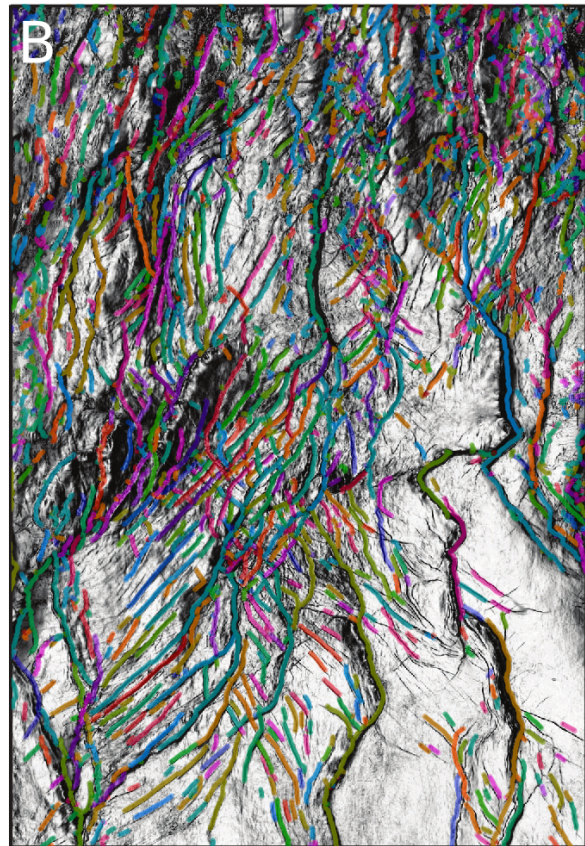
### 202 3.4. Comparison to conventional seismic interpretation

203 We can ask ourselves, “how good are our results compared to a state-of-the-art fault  
204 interpretation from the same data set using conventional fault mapping techniques?” (Fig. 8). Tillmans  
205 et al., (2021) map the Base Late Jurassic (base of syn-rift sediments associated with rift phase 2) on  
206 the eastern flank of the North Viking Graben (see Figs. 1A, 4 for location) using a combination of  
207 manual picking and auto-tracking on the same seismic dataset. This horizon is calibrated with 40  
208 exploration wells, which provide direct constraints on the depth of the surface. Tillmans et al. (2021)  
209 highlight the fault system by computing the variance attribute (Chopra and Marfurt, 2007) along the  
210 horizon (Fig. 7A). On top of the horizon, we plot the fault network mapped from the fault score  
211 extracted 500 m below the easily-mappable Base Cretaceous Unconformity (BCU) (Fig. 8B). This  
212 visual comparison shows that while we are missing a few faults in the southwest of the map, we are  
213 able to identify and accurately represent most of the faults identified by Tillmans et al. (2021). The  
214 missing faults are either overlooked by our model (i.e. false negatives) or result from the difference in  
215 the horizons that we compare: Base Cretaceous Unconformity (our study) versus Base Late Jurassic  
216 (Tillmans et al., 2021).

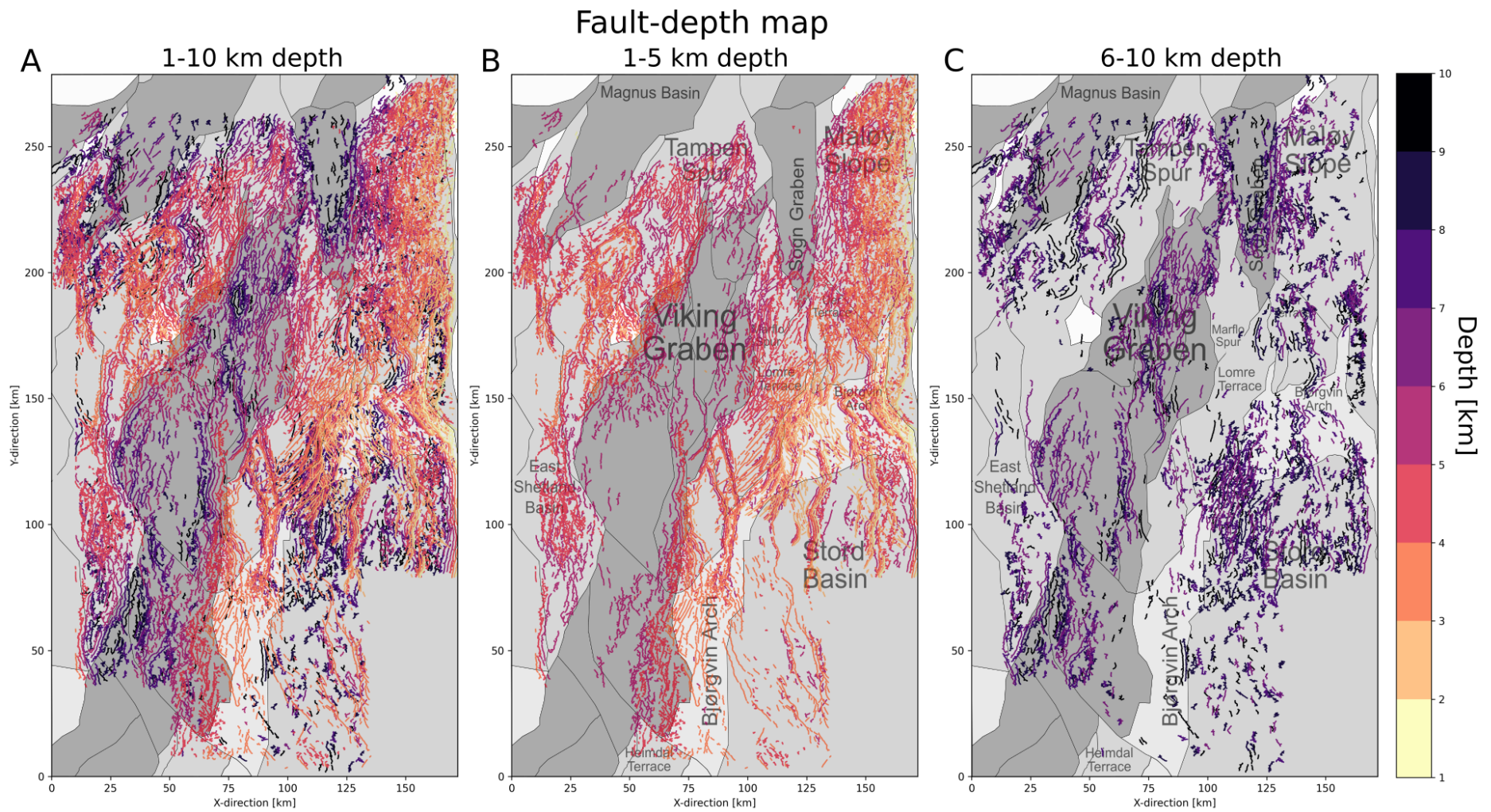
Time-structure map



+ extracted fault network

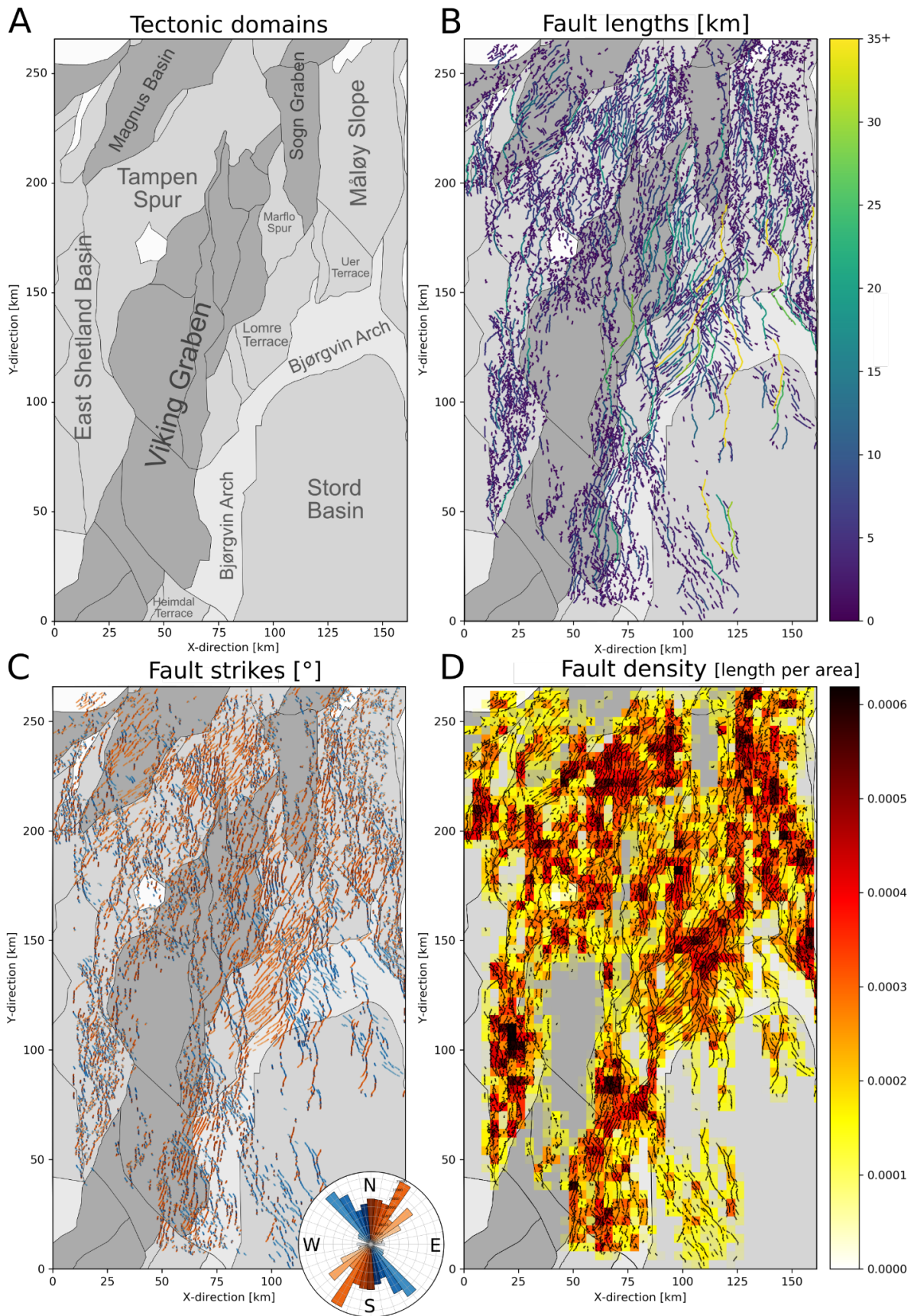
218  
219  
220  
221

**Figure 8:** Comparison of **A** Base Late Jurassic time-structure map interpreted by Tillmans et al., (2021) and **B** Automatically-extracted fault network 500 m below Base Cretaceous Unconformity using the same seismic dataset. Faults are distinguished by colour.



222  
223  
224

**Figure 9:** Fault map of the northern North Sea extracted every kilometre between 1-10 km depth (A), 1-5 km depth (B) and 6-10 km depth (C) with structural elements from the Norwegian Petroleum Directorate or NPD (2022).



225  
226  
227  
228

**Figure 10: A** Structural elements of the northern North Sea Rift (NPD, 2022) **B** Fault lengths (500 m below BCU) on top of structural elements. **C** Fault strikes (500 m below BCU) on top of structural elements with length-weighted Rose diagram. **D** Fault density on top of structural elements.



229  
230  
231  
232  
233  
234  
235  
236  
237  
238  
239  
240  
241  
242  
243  
244  
245

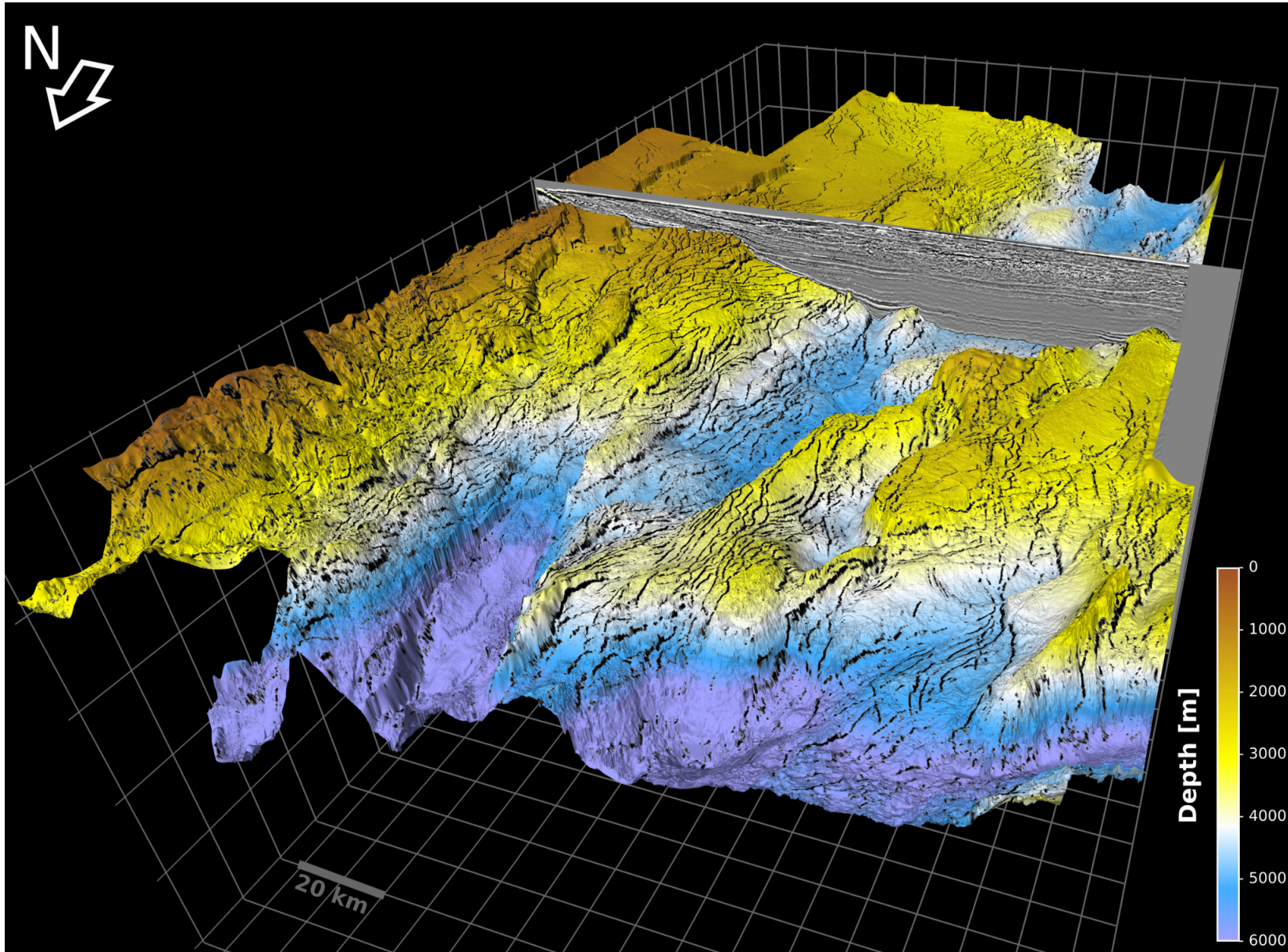


**Figure 11:** 3-D perspective of the northern North Sea rift showing the Base Cretaceous Unconformity overlain with faults (black) extracted from 3-D seismic reflection data with deep learning. Vertical exaggeration of 5.

## 246 4. OBSERVATIONS

247 Our fault extraction allows us to map a complex network consisting of 7983 individual faults  
248 across an approximately 161 km-wide and 266 km-long area, covering 35,410 km<sup>2</sup> of the northern  
249 North Sea rift (Fig. 7C).

### 250 4.1. Fault length

251 Faults vary in length by 3 orders of magnitude - from 50 m to 75.9 km, with some of the  
252 longest faults (>30 km) extending from the Stord Basin and Bjørgvin Arch in the south to the Uer and  
253 Lomre Terrace in the north (Fig. 10B). In cross-section, these faults have up to several kilometres of  
254 displacement and bound rotated half-graben (e.g. Whipp et al., 2014; Bell et al., 2014) (Fig. 3B,C).  
255 While we observe some long (up to 20 km) faults in the Viking Graben and Tampen Spur, most faults  
256 (>90%) are closely spaced (< 5 km) and relatively short (<10 km long) (Fig. 10B).

### 257 4.2. Fault strikes

258 In map view, we observe a complex network consisting of a large number of variably trending  
259 faults that display a broad range of intersection styles (e.g., oblique, perpendicular). These faults show  
260 a large range of strikes, varying from NW-SE to NE-SW (Figs. 9, 10C). The length-weighted rose  
261 plot shows that most faults strike NW-SE (light blue) or NNE-SSW (light orange), with a large  
262 number showing intervening strike directions (Fig. 10C). This general divide occurs between  
263 predominantly NW-SE-striking faults along the eastern part of the rift and NE-SW-striking faults in  
264 the central and northwestern part of the rift. This divide becomes most evident when comparing faults  
265 on the Lomre Terrace (NE-SW) to the adjacent Bjørgvin Arch (NW-SE), at least at the structural level  
266 of the Base Cretaceous Unconformity (Fig. 10C).

### 267 4.3. Fault density

268 In map view, we observe large variations in fault density 500 below the BCU (Fig. 10D). While  
269 dense networks of intersecting faults result in high density areas (e.g. Lomre Terrace, Bjørgvin Arch)  
270 we observe low densities in the Viking and Sogn Graben, where faults occur at greater depths (e.g.  
271 Fig. 9C).

#### 272 4.4. Vertical continuity

273           The faults extracted at different depths are variable in their vertical continuity (i.e., fault height;  
274 Fig. 8). Whereas some faults, in particular in the Stord Basin, the Tampen Spur, and the Magnus  
275 Basin show parallel fault traces from 1 to 10 km depth (Fig. 9A), we also observe a large number of  
276 faults that occur only at shallower (1-5 km) or at greater depths (6-10 km) (Fig. 9B, C). Upon closer  
277 inspection, we observe that the faults, which occur continuously between 1-10 km depth, e.g. in the  
278 eastern Stord Basin and the Bjørgvin Arch, are typically large-displacement normal faults with tens of  
279 kilometres spacing (e.g. Fig. 3B, C), whereas the other faults, which only occur between 6-10 km  
280 depth (e.g. northwestern Stord Basin), are usually shorter and more closely spaced (a few kilometres)  
281 (e.g. Fig. 9C).

282

283

### 284 5. DISCUSSION

#### 285 5.1. Advantages of deep learning based fault interpretation

286           When comparing our results to conventional interpretation methods, we can ask ourselves  
287 “what value does deep learning add?”. Here, we highlight the advantages of the supervised deep  
288 learning-based fault interpretation workflow which we present in this study. First, we can predict  
289 faults in a seismic section in a fraction of the time (5 seconds) required by expert interpreters (~10  
290 minutes). These differences accumulate, in particular when interpreting such a large data set with  
291 >22000 inlines. A conventional fault interpretation of such a large data set can take several months,  
292 whereas a trained convolutional neural network can identify faults across the entire volume within a  
293 day on a single GPU (GeForce GTX 1080 Ti). Note that this comparison does not include the time  
294 required to label the training data (~2 days), train the initial model (~4 hours), fine-tune and select the  
295 final model (days-months). Second, after identifying faults in seismic reflection data, they also need to  
296 be mapped before we can perform the relevant fault analysis. Here we map the fault network using a  
297 series of tools from computer vision and network analysis compiled in our fault analysis toolbox -  
298 fatbox (Wrona et al., 2022) (Figs. 6, 7). Our automated workflow extracts the fault network in less  
299 than five minutes compared to the several weeks to months that would have been required to

300 manually map the faults in this large data set. Furthermore, once extracted, we can immediately  
301 conduct a number of typical fault analyses using predefined functions implemented in fatbox (Wrona  
302 et al., 2022) (e.g. Fig. 10).

303 Third, conventional fault interpretations are often binary (fault vs. no fault), but deep learning delivers  
304 a score ranging from 0 (no fault) to 1 (fault). Although this score is no true fault probability (see  
305 discussion by Mosser and Naeini, 2022), the fault score nevertheless correlates with the visibility of  
306 faults (i.e. faults, which are well-resolved by the data, are associated with higher fault scores). This  
307 allows users to qualitatively select the faults that they want to analyze using a threshold (as done  
308 herein).. This selection is particularly useful for assessing the sealing potential of certain layers for  
309 CO<sub>2</sub> storage and for predicting fluid flow during geothermal exploration. Fourth, seismic interpreters  
310 typically focus on the largest faults, whereas our model performs the same prediction across the entire  
311 data set irrespective of the size of the faults encountered. Fifth, given the same data, labels, model and  
312 training, our model and results are fully reproducible, which is not the case for conventional fault  
313 interpretations, where the interpreter has to make a myriad of decisions in the process of mapping a  
314 fault network.

## 315 5.2. Complex fault system in the northern North Sea

316 Our study shows how to reveal the complex geometry of normal fault systems in 3-D seismic  
317 reflection data using a combination of deep learning and automated fault extraction. We were able to  
318 map an intricate network consisting of almost 8000 individual faults that cover an area approximately  
319 161 km wide and 266 km long (e.g. Figs. 4, 6, 10). This fault network shows large variations in fault  
320 length, strike and density, with extremely complex splays, junctions and intersections between these  
321 faults (Figs. 7-11). As such, our work goes far beyond typical seismic interpretations in previous case  
322 studies, which covered only a fraction of the rift (e.g. Duffy et al., 2015; Deng et al., 2017; Tillmans  
323 et al., 2021), or regional studies that mapped <100 of the largest faults using primarily sparse, 2-D  
324 seismic sections (e.g. Fig. 1B; Fazlikhani et al., 2017; Phillips et al., 2019).

### 325 5.3. Uncertainties during fault mapping

326 While there are several advantages to our approach, it is worth remembering the uncertainties  
327 associated with mapping faults in seismic reflection data. First, seismic reflection data can only image  
328 faults with displacement above the seismic resolution (and level of noise) of the data set. The seismic  
329 resolution of our data set decreases from 15 m (vertical) and 30 m (lateral) around 3 km depth down  
330 to 180 m (vertical) around 20 km depth (see Wrona et al., 2019; Tillman et al., 2021). Second, the  
331 labels we use to train our model are derived from 22 interpreted seismic sections, which, like any  
332 seismic interpretation, contains the expertise and biases of the interpreter (e.g. Bond et al., 2007, Bond  
333 2015). Third, the convolutional neural network that we trained achieves an accuracy of 83%, implying  
334 that 17% of the data is misclassified (see Wrona et al., 2021). A closer inspection reveals that 36% are  
335 false positives (i.e. faults that were overlooked) and 5% are false negatives (i.e. faults that were  
336 misinterpreted) (see Wrona et al., 2021). Despite these limitations, the robustness of our approach is  
337 evident when considering along-strike fault continuity across a large number of different seismic lines  
338 (Fig. 10, 11).

### 339 5.4. Future research on automated fault mapping

340 Based on our work, we can identify three related areas for future research. First, conventional  
341 neural networks predict a fault score from 0 to 1, which seems to correspond to the visibility of the  
342 fault in the dataset. Bayesian neural networks, on the other hand, allow the prediction of true fault  
343 probabilities (e.g. Mosser et al., 2020). Predicting fault probabilities in regional seismic data sets  
344 could significantly accelerate the screening for and risk assessment of potential CO<sub>2</sub> storage sites (see  
345 Wrona and Pan, 2021). Second, in addition to predicting where faults occur, we can explore the  
346 prediction of other fault properties, such as displacement, fault zone permeability or even the time  
347 when they were active. This would significantly allow us to study the spatial and temporal evolution  
348 of fault systems in high resolution at a regional scale. Third, while our fault extraction workflow  
349 currently focuses on mapping fault networks in a series of 2-D slices or horizons, we really need  
350 freely-available methods to generate 3-D fault surfaces, which allow for complex fault splays,  
351 junctions and intersections, as observed here.

## 352 6. CONCLUSIONS

353 This study shows that the combination of deep learning and network analysis applied to 3-D  
354 seismic reflection data allows us, for the first time, to map almost 8000 normal faults across the entire  
355 northern North Sea rift. These faults form an intricate network with complex relationships (e.g.  
356 splays, junctions, intersections) including large variations in fault length (50 m to 75.9 km) and strikes  
357 (NW-SE to NE-SW). As such, this work goes far beyond previous seismic studies by providing high  
358 resolution fault maps at a regional scale in a fraction of the time required by conventional  
359 interpretation methods.

## 360 ACKNOWLEDGEMENTS

361 We would like to thank The Norwegian Academy of Science and Letters (VISTA), The  
362 University of Bergen and The Initiative and Networking Fund of the Helmholtz Association through  
363 the project “Advanced Earth System Modelling Capacity (ESM), The Geo.X Network and Deutsche  
364 Forschungsgemeinschaft (Projektnummer 460760884) for supporting this research. I. Pan  
365 acknowledges the NUAcT fellowship for partially supporting the work. We are grateful to CGG, in  
366 particular Stein Åsheim and Jaswinder Mann, for the permission to present this data and publish this  
367 work. We thank Schlumberger for providing the software Petrel 2019© and Leo Zijerveld for IT  
368 support.

369

## 370 REFERENCES

- 371 Bartholomew, I.D., Peters, J.M., and Powell, C.M., 1993, Regional structural evolution of the North  
372 Sea: Oblique slip and the reactivation of basement lineaments, *in* Petroleum Geology  
373 Conference Proceedings, v. 4, p. 1109–1122, doi:10.1144/0041109.  
374 Bell, R.E., Jackson, C.A.L., Whipp, P.S., and Clements, B., 2014, Strain migration during multiphase  
375 extension: Observations from the northern North Sea: *Tectonics*, v. 33, p. 1936–1963,  
376 doi:10.1002/2014TC003551.  
377 Bissell, R.C., Vasco, D.W., Atbi, M., Hamdani, M., Okwelegbe, M., and Goldwater, M.H., 2011, A  
378 full field simulation of the In Salah gas production and CO<sub>2</sub> storage project using a coupled  
379 geo-mechanical and thermal fluid flow simulator: *Energy Procedia*, v. 4, p. 3290–3297.  
380 Bond, C.E., 2015, Uncertainty in structural interpretation: Lessons to be learnt: *Journal of Structural*  
381 *Geology*, v. 74, p. 185–200, doi:10.1016/j.jsg.2015.03.003.  
382 Brun, J.P., and Tron, V., 1993, Development of the North Viking Graben: inferences from laboratory  
383 modelling: *Sedimentary Geology*, v. 86, p. 31–51, doi:10.1016/0037-0738(93)90132-O.  
384 Chopra, S., and Marfurt, K.J., 2007, Seismic Attributes for Prospect Identification and Reservoir  
385 Characterization: Society of Exploration Geophysicists and European Association of

386 Geoscientists and Engineers, doi:10.1190/1.9781560801900.  
387 Claringbould, J.S., Bell, R.E., Jackson, C.A.L., Gawthorpe, R.L., and Odinsen, T., 2020, Pre-breakup  
388 Extension in the Northern North Sea Defined by Complex Strain Partitioning and  
389 Heterogeneous Extension Rates: *Tectonics*, v. 39, doi:10.1029/2019TC005924.  
390 Clerc, C., Jolivet, L., and Ringenbach, J.C., 2015, Ductile extensional shear zones in the lower crust  
391 of a passive margin: *Earth and Planetary Science Letters*, v. 431, p. 1–7,  
392 doi:10.1016/j.epsl.2015.08.038.  
393 Deng, C., Fossen, H., Gawthorpe, R.L., Rotevatn, A., Jackson, C.A.L., and FazliKhani, H., 2017,  
394 Influence of fault reactivation during multiphase rifting: The Oseberg area, northern North  
395 Sea rift: *Marine and Petroleum Geology*, v. 86, p. 1252–1272,  
396 doi:10.1016/J.MARPETGEO.2017.07.025.  
397 Doré, A.G., Lundin, E.R., Fichler, C., and Olesen, O., 1997, Patterns of basement structure and  
398 reactivation along the NE Atlantic margin: *Journal of the Geological Society*, v. 154, p. 85–  
399 92, doi:10.1144/gsjgs.154.1.0085.  
400 Duffy, O.B., Bell, R.E., Jackson, C.A.L., Gawthorpe, R.L., and Whipp, P.S., 2015, Fault growth and  
401 interactions in a multiphase rift fault network: Horda Platform, Norwegian North Sea: *Journal*  
402 *of Structural Geology*, v. 80, p. 99–119, doi:10.1016/J.JSG.2015.08.015.  
403 Færseth, R.B., 1996, Interaction of permo-triassic and jurassic extensional fault-blocks during the  
404 development of the northern North Sea: *Journal of the Geological Society*, v. 153, p. 931–  
405 944, doi:10.1144/gsjgs.153.6.0931.  
406 Færseth, R.B., Knudsen, B.E., Liljedahl, T., Midbøe, P.S., and Söderstrøm, B., 1997, Oblique rifting  
407 and sequential faulting in the Jurassic development of the northern North Sea: *Journal of*  
408 *Structural Geology*, v. 19, p. 1285–1302, doi:10.1016/s0191-8141(97)00045-x.  
409 Fazlikhani, H., Fossen, H., Gawthorpe, R.L., Faleide, J.I., and Bell, R.E., 2017, Basement structure  
410 and its influence on the structural configuration of the northern North Sea rift: *Tectonics*, v.  
411 36, p. 1151–1177, doi:10.1002/2017TC004514.  
412 Guo, Z., and Hall, R.W., 1992, Fast fully parallel thinning algorithms: *CVGIP: Image Understanding*,  
413 v. 55, p. 317–328, doi:10.1016/1049-9660(92)90029-3.  
414 Kampman, N., Bickle, M., Wigley, M., and Dubacq, B., 2014, Fluid flow and CO<sub>2</sub>–fluid–mineral  
415 interactions during CO<sub>2</sub>-storage in sedimentary basins: *Chemical Geology*, v. 369, p. 22–50.  
416 Lohr, T., Krawczyk, C.M., Oncken, O., and Tanner, D.C., 2008, Evolution of a fault surface from 3D  
417 attribute analysis and displacement measurements: *Journal of Structural Geology*, v. 30, p.  
418 690–700, doi:10.1016/j.jsg.2008.02.009.  
419 Maystrenko, Y.P., Olesen, O., Ebbing, J., and Nasuti, A., 2017, Deep structure of the northern north  
420 sea and southwestern Norway based on 3D density and magnetic modelling: *Norsk Geologisk*  
421 *Tidsskrift*, v. 97, p. 169–210, doi:10.17850/njg97-3-01.  
422 Moeck, I., Kwiatek, G., and Zimmermann, G., 2009, Slip tendency analysis, fault reactivation  
423 potential and induced seismicity in a deep geothermal reservoir: *Journal of Structural*  
424 *Geology*, v. 31, p. 1174–1182.  
425 Morris, A., Ferrill, D.A., and Henderson, D.B., 1996, Slip-tendency analysis and fault reactivation:  
426 *Geology*, v. 24, p. 275–278.  
427 Mosser, L., Purves, S., and Naeini, E.Z., 2020, Deep bayesian neural networks for fault identification  
428 and uncertainty quantification: 1st EAGE Digitalization Conference and Exhibition,  
429 doi:10.3997/2214-4609.202032036.  
430 Mosser, L., and Naeini, E.Z., 2022, A comprehensive study of calibration and uncertainty  
431 quantification for Bayesian convolutional neural networks — An application to seismic data,  
432 *GEOPHYSICS* 87: IM157-IM176. <https://doi.org/10.1190/geo2021-0318.1>  
433  
434 Naliboff, J.B., Glerum, A., Brune, S., Péron-Pinvidic, G., and Wrona, T., 2020, Development of 3D  
435 rift heterogeneity through fault network evolution: *Geophysical Research Letters*,  
436 doi:10.1029/2019gl086611.  
437 Osagiede, E.E., Rotevatn, A., Gawthorpe, R., Kristensen, T.B., Jackson, C.A., and Marsh, N., 2020,  
438 Pre-existing intra-basement shear zones influence growth and geometry of non-colinear  
439 normal faults, western Utsira High–Heimdal Terrace, North Sea: *Journal of Structural*  
440 *Geology*, v. 130, p. 103908.

441 Pan, S., Naliboff, J., Bell, R.E., and Jackson, C., 2021, Bridging spatiotemporal scales of normal fault  
442 growth using numerical models of continental extension: EarthArXiv,  
443 doi:10.31223/X5DG7M.

444 Phillips, T.B., Fazlikhani, H., Gawthorpe, R.L., Fossen, H., Jackson, C.A.L., Bell, R.E., Faleide, J.I.,  
445 and Rotevatn, A., 2019, The Influence of Structural Inheritance and Multiphase Extension on  
446 Rift Development, the Northern North Sea: *Tectonics*, v. 38, p. 4099–4126,  
447 doi:10.1029/2019TC005756.

448 Tillmans, F., Gawthorpe, R.L., Jackson, C.A. -L., and Rotevatn, A., 2021, Syn-rift sediment gravity  
449 flow deposition on a Late Jurassic fault-terraced slope, northern North Sea: *Basin Research*,  
450 v. 33, p. 1844–1879, doi:10.1111/BRE.12538.

451 Torsvik, T.H., Andersen, T.B., Eide, E.A., and Walderhaug, H.J., 1997, The age and tectonic  
452 significance of dolerite dykes in western Norway: *Journal of the Geological Society*, v. 154,  
453 p. 961–973, doi:10.1144/gsjgs.154.6.0961.

454 Whipp, P.S., Jackson, C.A.L., Gawthorpe, R.L., Dreyer, T., and Quinn, D., 2014, Normal fault array  
455 evolution above a reactivated rift fabric; a subsurface example from the northern Horda  
456 Platform, Norwegian North Sea: *Basin Research*, v. 26, p. 523–549, doi:10.1111/bre.12050.

457 Wiest, J.D., Wrona, T., Bauck, M.S., Fossen, H., Gawthorpe, R.L., Osmundsen, P.T., and Faleide, J.I.,  
458 2020, From Caledonian Collapse to North Sea Rift: The Extended History of a Metamorphic  
459 Core Complex: *Tectonics*, v. 39, doi:10.1029/2020TC006178.

460 Wrona, T., Brune, S., Gayrin, P., and Hake, T., 2022, Fatbox - Fault Analysis Toolbox: GFZ Data  
461 Services, doi:10.5880/GFZ.2.5.2022.002.

462 Wrona, T., Magee, C., Fossen, H., Gawthorpe, R.L.L., Bell, R.E.E., Jackson, C.A.-L.A.L., and  
463 Faleide, J.I.I., 2019, 3-D seismic images of an extensive igneous sill in the lower crust:  
464 *Geology*, v. 47, p. 729–733, doi:10.1130/G46150.1.

465 Wrona, T., Magee, C., Jackson, C.A.L.C.A.-L.C.A.L., Huuse, M., and Taylor, K.G.K.G., 2017,  
466 Kinematics of polygonal fault systems: Observations from the northern north sea: *Frontiers in*  
467 *Earth Science*, v. 5, p. 101, doi:10.3389/feart.2017.00101.

468 Wrona, T., and Pan, I., 2021, Can machine learning improve carbon storage? Synergies of deep  
469 learning, uncertainty quantification and intelligent process control:

470 Wrona, T., Pan, I., Bell, R.E., Gawthorpe, R.L., Fossen, H., and Brune, S., 2021a, 3D seismic  
471 interpretation with deep learning: A brief introduction: *Society of Exploration Geophysicists*,  
472 v. 40, p. 524–532, doi:10.1190/tle40070524.1.

473 Wrona, T., Pan, I., Bell, R.E., Gawthorpe, R.L., Fossen, H., and Brune, S., 2021b, 3-D seismic  
474 interpretation with deep learning: a set of Python tutorials:, doi:10.5880/GFZ.2.5.2021.001.

475 Wu, X., Liang, L., Shi, Y., and Fomel, S., 2019, FaultSeg3D: Using synthetic data sets to train an end-  
476 to-end convolutional neural network for 3D seismic fault segmentation: *GEOPHYSICS*, v.  
477 84, p. IM35–IM45, doi:10.1190/geo2018-0646.1.

478 Wu, K., Otoo, E., and Suzuki, K., 2009, Optimizing two-pass connected-component labeling  
479 algorithms: *Pattern Analysis and Applications*, v. 12, p. 117–135, doi:10.1007/S10044-008-  
480 0109-Y.

481 Yukutake, Y., Takeda, T., and Yoshida, A., 2015, The applicability of frictional reactivation theory to  
482 active faults in Japan based on slip tendency analysis: *Earth and Planetary Science Letters*, v.  
483 411, p. 188–198.